Corrected 2 February 2024. See full text.

NATURAL HAZARDS

Supershear triggering and cascading fault ruptures of the 2023 Kahramanmaraş, Türkiye, earthquake doublet

Chunmei Ren[1]†, Zexin Wang[1]†, Tuncay Taymaz[2], Nan Hu[3], Heng Luo[1], Zeyan Zhao[1], Han Yue[1]*, Xiaodong Song[1,4]*, Zhengkang Shen[5,1], Haoyu Xu[1], Jianghui Geng[6], Wei Zhang[3], Teng Wang[1], Zengxi Ge[1], T. Serkan Irmak[7], Ceyhun Erman[2], Yijian Zhou[8], Zhen Li[1], Hang Xu[1], Bonan Cao[1], Hongyang Ding[1]

On 6 February 2023, two large earthquakes (moment magnitude 7.8 and 7.6) shocked a vast area of southeastern Türkiye and northern Syria, leading to heavy casualties and economic loss. To investigate the rupture process over multiple fault segments, we performed a comprehensive analysis of local seismic and geodetic data and determined supershear ruptures on the initial branch and the Pazarcık and Erkenek segments and subshear ruptures on the Amanos segment of event 1. The bilateral rupture of event 2 also presents distinct sub- and supershear velocities. The dynamic stress of the branch fault rupture triggered the Pazarcık segment initial rupture at a point 9 kilometers west of the junction of these two faults, boosting the supershear rupture of the Pazarcık segment of the main fault. The geometry and prestress level of multiple segments controlled the rupture behaviors and influenced the ground shaking intensity.

On 6 February 2023, a devastating earthquake of moment magnitude (M_w) 7.8 ("event 1") near the city of Kahramanmaraş shocked southeastern Türkiye and northern Syria. The event was initiated at 04:17:34 a.m. local time [or 01:17:34 UTC, per the United States Geological Survey (USGS)], and it lasted for ~90 s and produced ~380-km-long surface ruptures. Event 1 was followed by another major event of M_w 7.6 ("event 2") about 9 hours later (at 10:24:48 UTC, per the USGS), which produced ~200-km surface ruptures along a separate fault located ~100 km north of the event 1 epicenter (Fig. 1A). This 2023 Kahramanmaraş earthquake doublet resulted in catastrophic destruction with substantial devastation to a populated area covering several major cities in southeastern Türkiye and northwestern Syria (e.g., Kahramanmaraş, Adıyaman, Şanlıurfa, Antakya, Gaziantep, Malatya, İskenderun, and Adana, among others) and caused more than 50,000 deaths and 100,000 injuries across both countries. The total economic loss is estimated to be >100 billion USD. Event 1 is one of the largest continental strike-slip events recorded by modern seismological instruments, comparable to the 2001 M_w 7.8 Kokoxili earthquake (*1*), the 2002 M_w 7.8 Denali earthquake (*2*), and the 1906 M_w 7.7–7.8 San Francisco earthquake (*3*). The doublet is the largest continental earthquake doublet ever recorded by modern seismological instruments (*4*).

The 2023 Kahramanmaraş earthquake doublet (Fig. 1) occurred in the East Anatolian Fault Zone (EAFZ), which is a major fault zone created by the oblique collision between the Anatolian and Arabian plates. The regional tectonic setting is controlled by the interaction between the Anatolian plate and the surrounding Eurasian, African, and Arabian plates (*5*–*7*). Aside from the continental collision, the subduction of the African plate also leads to the opening of the Aegean Sea (*6*, *8*), and the net force of collision and dilatation causes a westward movement of the Anatolian plate, resulting in the formation of two major fault systems along its northern and eastern boundaries: the North Anatolian Fault Zone (NAFZ) and the EAFZ (*7*, *9*). The NAFZ slips at a high rate of between 18 and 22 mm/year (*10*) and has produced high seismic activity along the fault during the 20th century (*11*, *12*) (Fig. 1A). The EAFZ slips at a relatively lower rate: ~10 mm/year on its central to northeastern (from Nurdağı-Pazarcık to Pütürge) segments and ~4.5 mm/year on its southwestern (Amanos) segment (Fig. 1). The EAFZ was ruptured by several historical events before the 20th century, including the 1513 M 7.4, 1822 M 7.5, 1866 M 7.2, 1874 M 7.1, and 1893 M 7.1 events (*13*) (Fig. 1B), but it was relatively inactive in the 20th century and the first two decades of the 21st century, until an M_w 6.8 event ruptured the Pütürge segment of the fault in 2020 (*14*).

Segmented rupture appears to be the main characteristic of both fault zones, which indicates that junctions of segments—for example, stepover, bending, and intersections—serve as barriers to stop dynamic ruptures (*13*). However, a large earthquake may break through these barriers and sequentially rupture several segments, as occurred during the 1668 Anatolian earthquake (*15*) (Fig. 1A). Event 1 of the 2023 doublet is also such an event; it ruptured three segments (Amanos, Pazarcık, and Erkenek) hosting three historical events (1822, 1513, and 1893 events). This behavior of multiple segment ruptures poses a challenge for forecasting the earthquake potential of the region (*16*). Meanwhile, supershear rupture is commonly found in large strike-slip events (*17*), in which the rupture propagation velocity exceeds the shear wave velocity, causing intensive ground shaking in the surrounding region. Of particular interest in the 2023 Kahramanmaraş doublet is the role that supershear rupture may have played in triggering multisegment ruptures. The near-fault seismic and geodetic observations available for this doublet provide us with an unprecedented opportunity to determine the multisegment triggering mechanism and ground shaking intensity from a perspective of rupture kinematics.

Faulting geometry and slip model

As continental earthquakes, the surface rupture and ground deformation of the 2023 Kahramanmaraş doublet were well monitored by seismic and geodetic observations. From various synthetic aperture radar (SAR) interferograms and optical images, we constructed three-dimensional (3D) ground deformation of coseismic slips from azimuth, range, and pixel offsets [Fig. 2A; see section S1.4 in (*18*)]. Surface ruptures are well mapped by these images. Event 1 rupture covers a lateral extent of ~380 km, spanning the Amanos ("Seg A"), Pazarcık ("Seg P"), and Erkenek ("Seg E") segments, with surface offsets (averaged for fault traces with > 0.1 m coseismic offsets) of 1.5, 2.8, and 2.1 m resolved on each segment, respectively. A subfault parallel to Seg A is consistent with a branch of aftershock lineation and hypocenter location, which appears to be the initial branch (Nurdağı fault) that hosts the hypocenter and triggered the cascading rupture on the other segments (Fig. 2, A and B). The surface rupture of event 2 is also imaged by the SAR data, which extends ~200 km in the east-west direction spanning the Sürgü, Çardak, and Savrun segments. The epicenter is located at the center of surface rupture, representing a bilateral rupture.

To determine the geometry of fault orientation at depth, we performed a multi-point-source (MPS) inversion (*19*) using teleseismic body waves [section S1.6 in (*18*)]. This method decomposes the kinematic rupture process into sequential ruptures of a cluster of point sources

[1]School of Earth and Space Sciences, Peking University, Beijing 100871, China. [2]Department of Geophysical Engineering, The Faculty of Mines, Istanbul Technical University, 34467 Sarıyer, Istanbul, Türkiye. [3]Department of Earth and Space Sciences, Southern University of Science and Technology, Shenzhen, Guangdong 518055, China. [4]SinoProbe Laboratory, School of Earth and Space Sciences, Peking University, Beijing 100871, China. [5]Department of Earth, Planetary, and Spaces Sciences, University of California, Los Angeles, CA 90095, USA. [6]GNSS Research Center, Wuhan University, Wuhan 430079, China. [7]Department of Geophysical Engineering, Faculty of Engineering, Kocaeli University, 41380 Umuttepe, Kocaeli, Türkiye. [8]Department of Earth and Planetary Sciences, University of California, Riverside, CA 92521, USA.
***Corresponding author. Email: yue.han@pku.edu.cn (H.Y.); xiao.d.song@gmail.com (X.S.)**
†These authors contributed equally to this work.

Corrected 2 February 2024. See full text.

whose locations and focal mechanisms reflect the fault planes and slips of different segments. The MPS results are consistent with the branch initiation and bilateral rupture of event 1. The high-dip angles of all the MPS solutions for the doublet suggest that the hosting faults are mostly subvertical (Fig. 2 and tables S8 and S9). This feature is also consistent with the relocated aftershocks at depth (Fig. 2B and figs. S8 and S9). Considering the above evidence and focal mechanisms of background seismicity (*20*), we parameterized the faults to be vertical above 10 km and dipping slightly to the northwest direction (between 80° and 85° for different segments) at deeper depths.

The 2023 Kahramanmaraş doublet was well recorded by numerous near-field monitoring stations of various types (Fig. 2A), allowing for a joint inversion of the rupture process using regional strong motion (SM) (table S2), high-rate GPS, static GPS (table S3), and SAR images (table S4). The joint inversion technique exploits the complementary resolution of different datasets (*21*), yielding finite-fault models (FFMs) of both events with robust spatial-temporal resolutions. We also obtained the slip models of the two events simultaneously (Fig. 2C) [section S2.1 in (*18*)], to take advantage of the high spatial resolution of the SAR images (*22*, *23*). We performed a hypocenter relocation for event 1 and set the hypocenter at 37.003°N, 37.235°E, 12.6 km depth, at 1:17:33 UTC, for the FFM inversion. Note that the hypocentral location and timing have a substantial impact on the kinematic rupture models, especially for the initial branch [section S1.5 in (*18*)]. Hereafter, we use timing relative to the hypocenter to describe the rupture process.

For event 1, the rupture started at the southwest of the initial branch, propagated unilaterally to the northeast, triggered Seg P rupture at about 11 s, and was followed by the subsequent bilateral rupture propagation. In the northeast direction, the rupture broke through the Seg P and E junction and continued along Seg E for about 60 km. The major asperity (a locked area of high prestress that is released during an earthquake) was located near the junction between the initial branch and Seg P with a peak slip of ~12 m. Another asperity with a peak slip of ~10 m was identified at the center of Seg E. Although the slips on Seg P and E seem continuous in all ruptured portions, the slip amounts vary substantially. To the southwest direction, the rupture broke the whole of Seg A for ~150 km, on which we observe two main asperities, located 70 and 120 km from the junction, with peak slips of ~6 and ~9 m, respectively. The initial rupture of event 2 was located at the center of the Çardak fault and propagated bilaterally. Its rupture terminated at the western end of the Savrun fault and the eastern end of the Sürgü fault, which bent to the southwest and northeast directions, respectively. The event 2 rupture is distributed more on the Savrun fault than on the Sürgü fault, with a peak slip of ~12 m near the hypocenter (Fig. 2C).

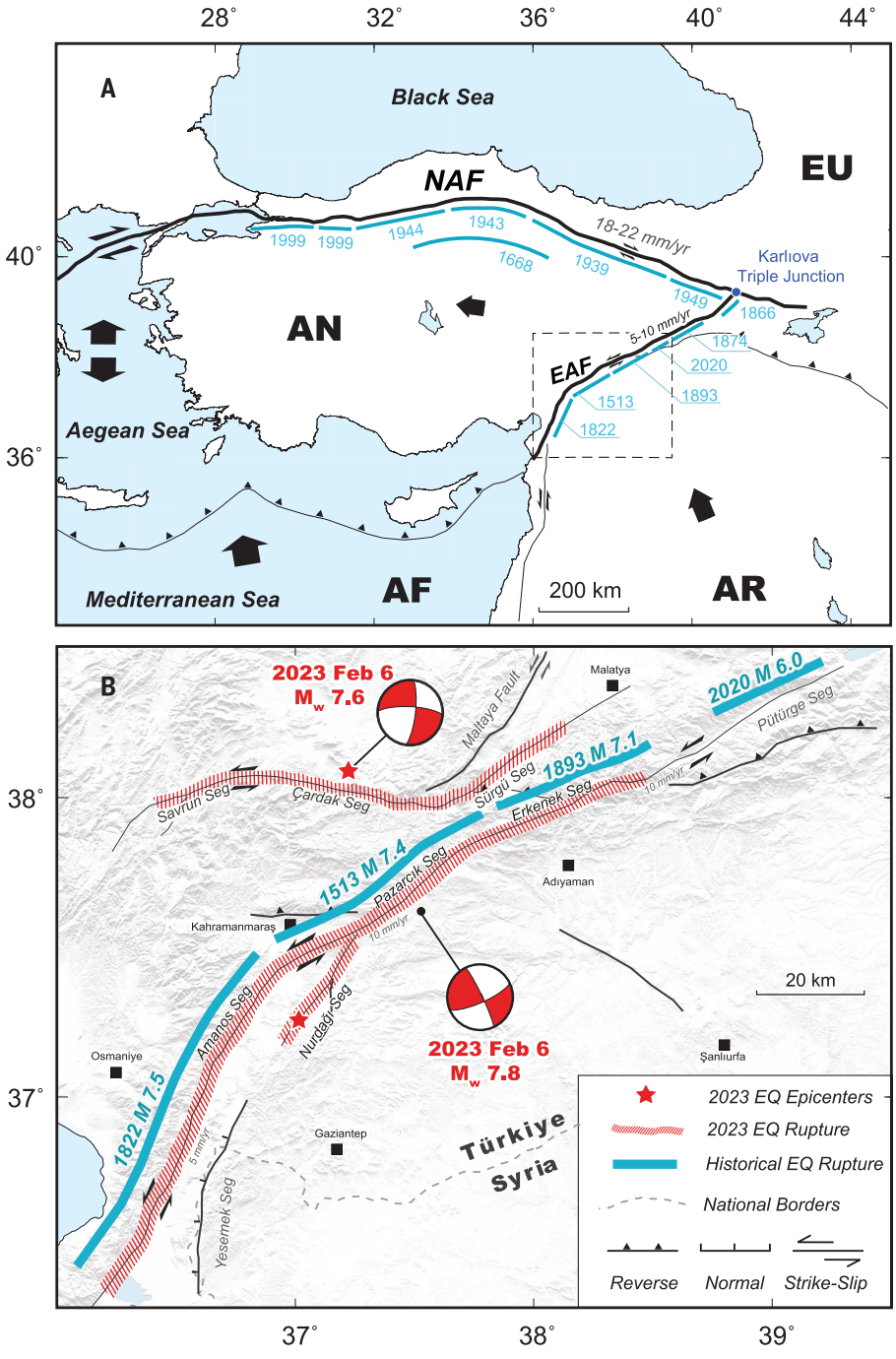

Fig. 1. Maps of faults and earthquakes in the region. (**A**) Regional tectonic setting. Eurasian (EU), Anatolian (AN), African (AF), and Arabian (AR) plates are labeled, with their relative moving directions marked by arrows. The North and East Anatolian Faults are labeled (NAF and EAF, respectively), and the ruptures of large historical earthquakes are marked with blue bars. (**B**) Magnification of the region marked with a dashed box in (A). Seismogenic faults of the 2023 southeastern Türkiye doublet. Ruptured segments of the doublet are marked as red-hatched segments. Moment focal mechanisms of major events during the 2023 sequence are plotted as red-and-white beach balls.

A clear complementary pattern between the distributions of aftershocks (*24*) and coseismic slips was found for both events, but details vary by segment. Aftershocks on Seg P and E were mostly located near the bottom of coseismic rupture, whereas aftershocks on Seg A were more concentrated between asperities,

Corrected 2 February 2024. See full text.

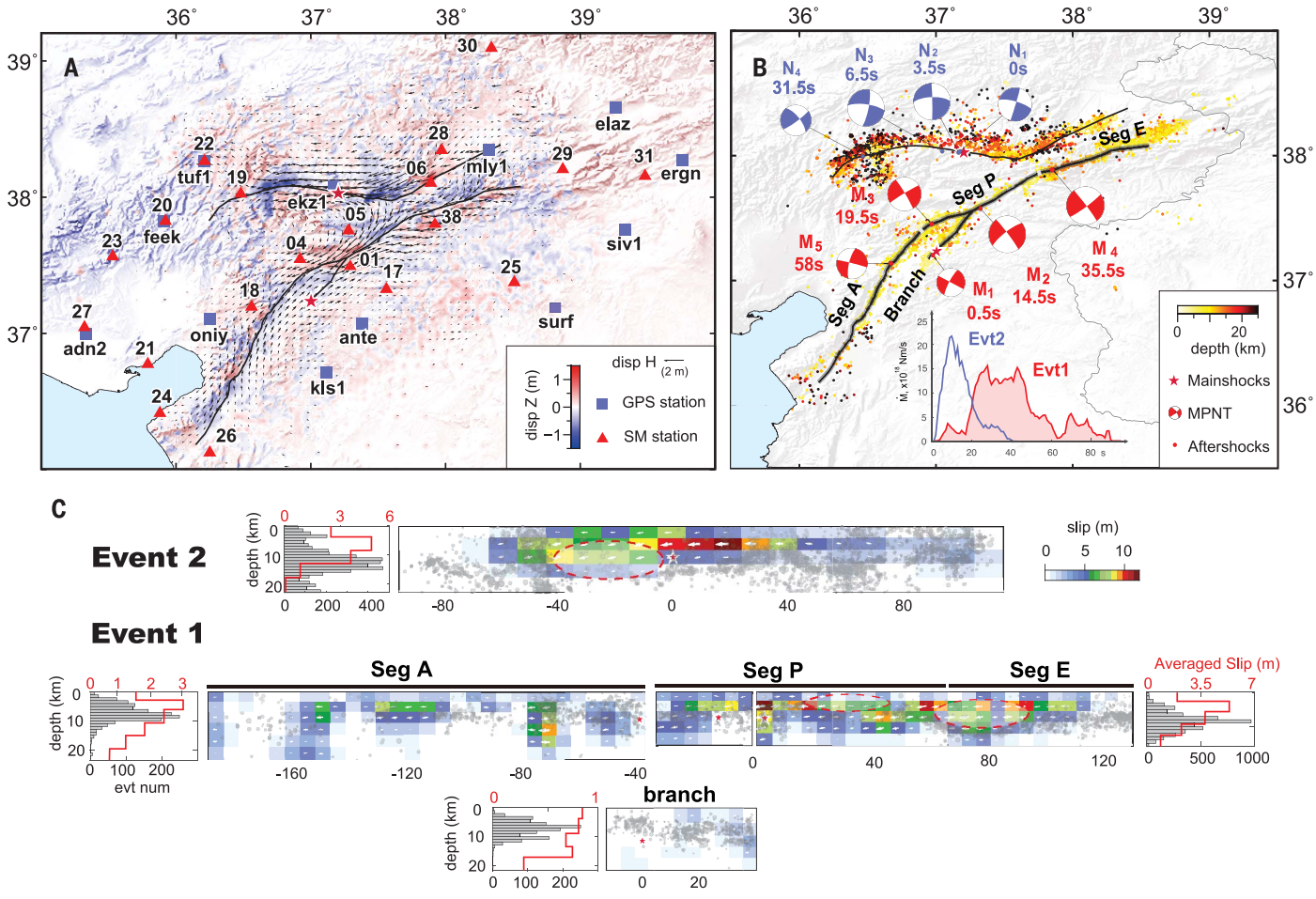

Fig. 2. Coseismic deformation and slip models. (**A**) Coseismic vertical ground uplift (colors) and horizontal displacements (arrows) at the surface. Fault traces are identified from the surface offsets (black curves). Other symbols represent the hypocenters of the doublet (red stars), GPS stations; blue squares), and SM stations (red triangles; assigned names listed in table S2) used in FFM inversion. (**B**) Earthquake and fault rupture data: rupture segments (lines), MPS inversion focal mechanisms (beach balls), and relocated aftershocks (colored dots). The inset shows the source time function of the doublet. The fault segments for event 1 are labeled for the initial branch ("Branch"), Pazarcık ("Seg P"), Amanos ("Seg A"), and Erkenek ("Seg E"). The MPS results are marked as M_1 to M_5 for event 1 and N_1 to N_4 for event 2. (**C**) Slip distributions (colors) of the doublet on the fault segments, along with initiation points of each segment (red stars) and the aftershock distributions (gray dots). The histograms on the side show the depth distribution of the aftershocks (gray filled histogram) and the averaged slip distribution (red curve) along the depth profile in each segment. Voids of aftershocks are marked as dashed red ellipses.

causing different depth concentrations (shallower for Seg A and deeper for Seg P and E) (Fig. 2C). The on-fault aftershocks were related to the stress concentration on the lateral and bottom edges of the asperities, whereas the asperities on Seg A were more scattered, with ruptures being large at shallow depths. We observed two voids of aftershocks on the central Seg P of event 1 and the western portion of event 2 (Fig. 2C), which may be related to supershear rupture behavior that will be discussed in the next section.

Detailed rupture kinematics

The 2023 Kahramanmaraş doublet displays distinctive features in its rupture kinematics (Fig. 3), which illustrate the spatial-temporal evolution of the rupture front over multiple fault segments. The rupture kinematics of event 1 are well constrained by the analysis of the SM data and the joint inversion results (Fig. 3, fig. S13, and table S13).

For event 1, several SM stations are well distributed along Seg A for recording and deciphering fault ruptures, but SM stations located around the initial branch and Seg P and Seg E are not as suitably located, thus making it necessary to use different techniques to analyze the data. For the initial branch, we analyzed the waveforms of two near-fault stations, 01 and 02, which exhibit supershear rupture [section S3.1 in (*18*)]. A pre-hypocentral *S*-wave arrival is identified at station 01 (Fig. 3E), which requires a supershear rupture of the initial branch. Three main asperities are identified from our slip model of the initial branch (Fig. 2 and fig. S19). By carefully examining waveforms at station 01, we identify *P* and *S* phases that are associated with the start and termination of asperity 1 near the hypocenter (fig. S18). Using the relative *S* and *P* times and assuming a straight path of along-fault rupture propagation (1D path), we determined a rupture velocity (V_r) of about 4.0 km/s. A more realistic assumption is a rupture propagation along asperities distributed on the fault plane (2D path). In this case, the along-path V_r is estimated even higher (4.9 to 5.4 km/s; figs. S19 and S20) from asperity 1 to asperity 3 (close to the junction). Given that the upper-crust shear velocity of this region is ~3.6 km/s (*25*), the averaged V_r is well located in the supershear domain no matter which propagation path is assumed [section S3.1 in (*18*)]. Another path is also identified with an upward propagation from asperity 1 to asperity 2 (near the center of the initial branch), which has a distinct subshear V_r (2.6 to 3.0 km/s).

Corrected 2 February 2024. See full text.

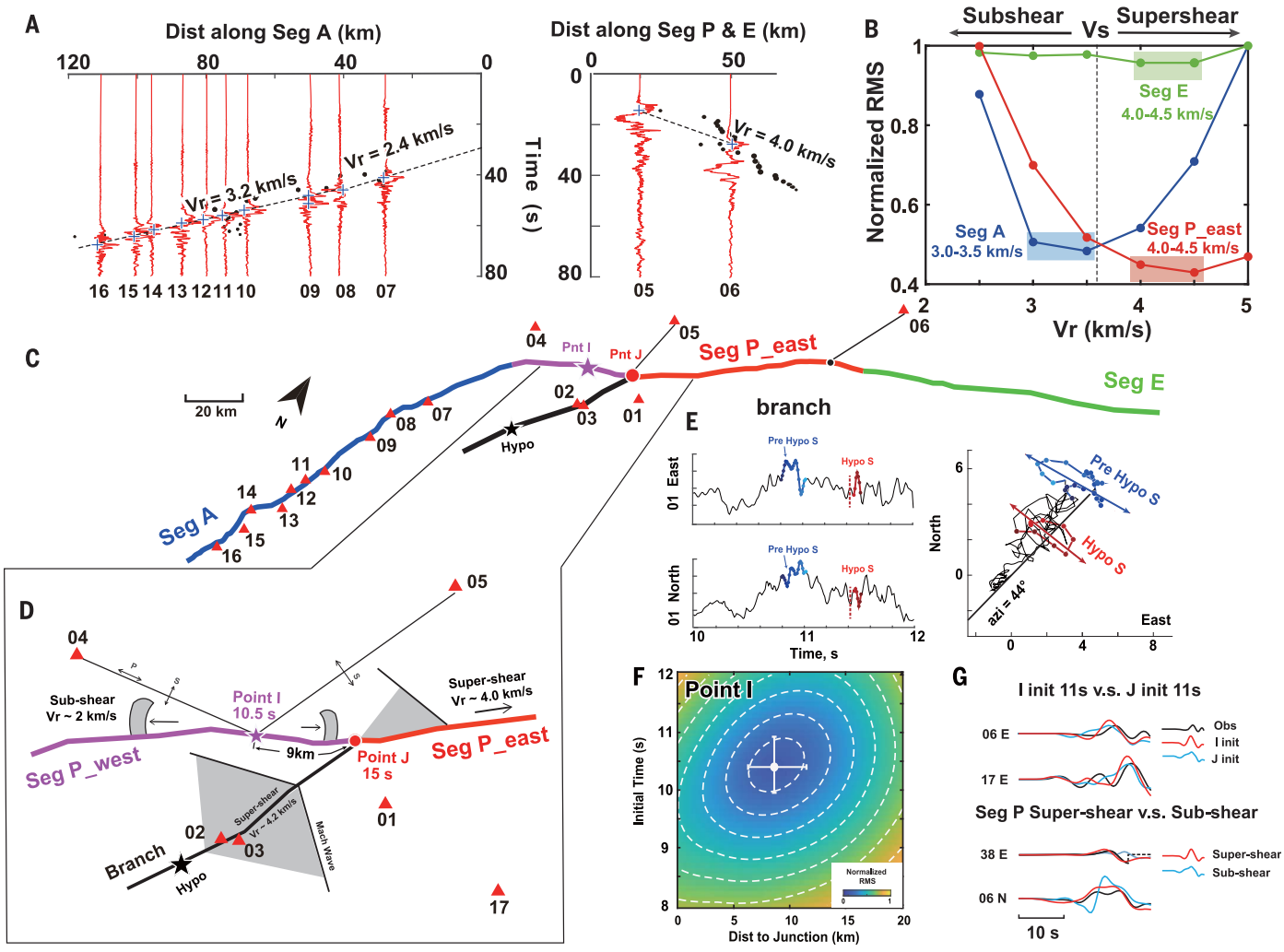

Fig. 3. Analyses of event 1 rupture kinematics. (**A**) SM stations near the fault segments (Seg A, P, and E) whose data are used to estimate the rupture velocities (V_r). The stations are labeled and shown in (C). Rupture arrival times are estimated from peaks of the fault-parallel velocity (blue crosses). The dashed lines indicate linearly fitted V_r from the peak arrivals. (**B**) Estimates of V_r from trade-off curves of residual root mean square (RMS) with V_r in the joint inversion. The curves for Seg A, P, and E are plotted using identical color coding as in (C). The estimated ranges of the optimal V_r are shaded and labeled for each segment. (**C**) Fault segments (colors) of event 1, along with other information, including nearby SM stations (red triangles), hypocenter (black star), the initial point I of Seg P (purple star), and junction point J (red dot). (**D**) Magnified view of the initial branch and Seg P for V_r analyses. Areas swept by sub- and supershear wavefronts are illustrated by gray curved shading (upper left) and triangular shading (upper right and bottom), together with estimated V_r values. (**E**) Horizontal ground velocity waveforms (east and north) (left) and particle motions (right) of station 01. Two *S*-wave arrivals are marked, from the hypocenter (red) and a pre-hypocentral arrival (blue). (**F**) Data post-fit residual distribution of station 01 for the initial time and location of point I. The optimized solution and uncertainties are marked with a white cross. (**G**) Waveform comparison for different kinematic parameters. Examples of waveforms show the observed (black) and synthetic waveforms for different initial points (I and J in red and cyan, respectively) and V_r values (super- and subshear in red and cyan, respectively) on the top and bottom panels, respectively.

The discrepancy between the two paths is expected for the respective rupture modes whose paths are parallel and normal to the slip direction (*26*).

Intuitively, the initial branch rupture should have reached the junction (point J) first and triggered subsequent rupture to propagate bilaterally on Seg P. However, the rupture sequence on Seg P is quite complicated. The sequence and triggering mechanism of the rupture from the branch to Seg P are a key part of the rupture process of event 1, which we determined as follows. First, the rupture on Seg P was initiated at another location, about 9 km west of the junction at about 10.5 s after the start of the event [point I, Fig. 3F; section S3.2 in (*18*)]. By analyzing waveform polarity and amplitude of two near-field stations (stations 04 and 05; Fig. 3D and fig. S21), we obtained the particle motion and arrival times of *P* and *S* phases of the Seg P initial rupture, and by backtracking along the ray path and fitting the arrival times of both phases, we could pin down the Seg P initial rupture (point I). This result is also consistent with a 2D grid search for the initial point of Seg P in FFM inversions (fig. S25). Our theoretical travel time calculation using the FFM suggests that the supershear rupture of the initial branch sent out a Mach wave subparallel to the southwest portion of Seg P (fig. S25), which arrived at points I and J in sequence within a short time (between 9 and 10 s). The initiation of point I rupture is likely associated with the Mach wave arrival. Incorporating a numerical simulation experiment (*27*, *28*), we calculated the dynamic stress field caused by the initial branch rupture and found a peak coulomb stress impulse at point I (~1.4 MPa) at ~9.5 s, which is consistent with

Corrected 2 February 2024. See full text.

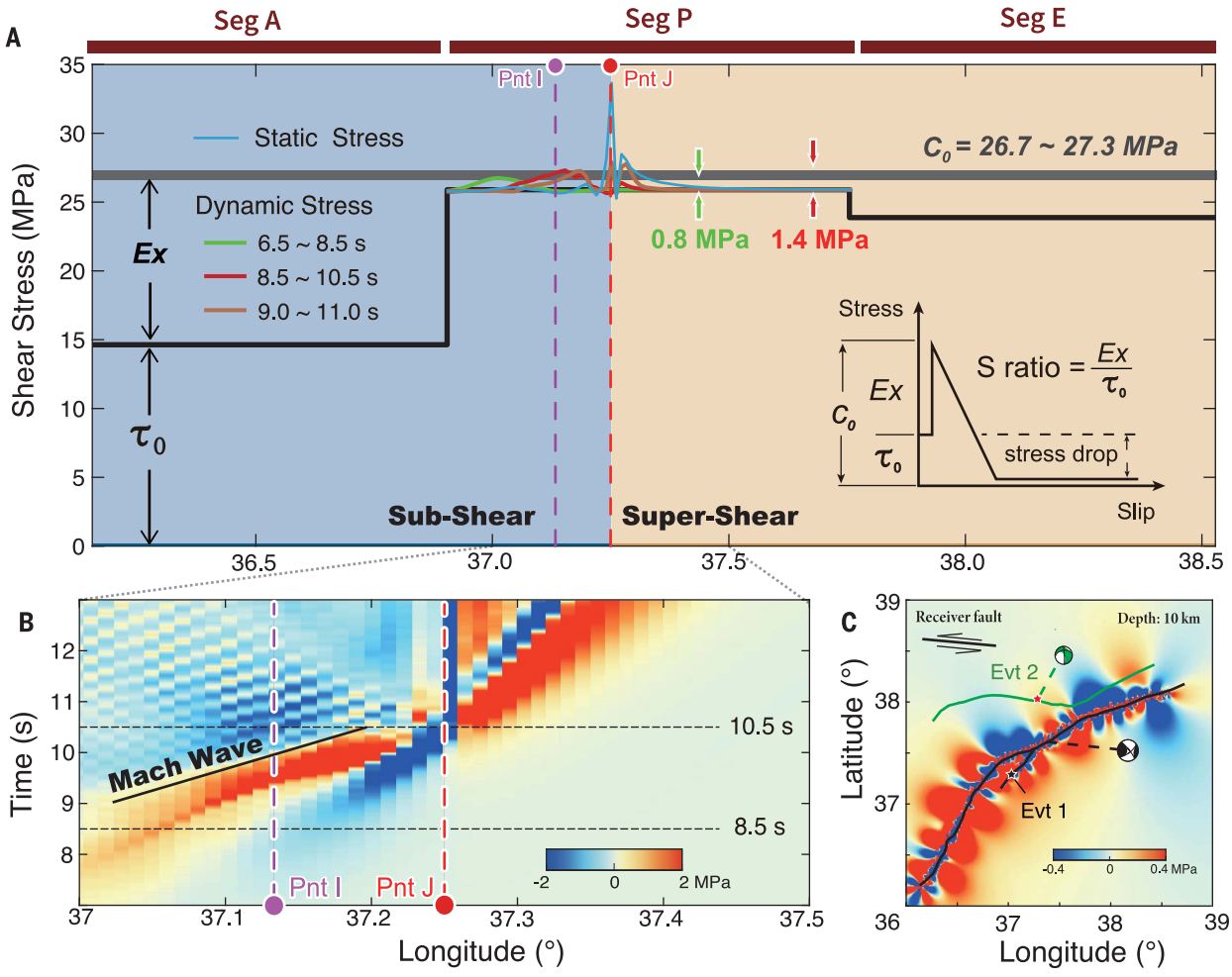

Fig. 4. Stresses on the fault segments. (**A**) Along-strike distribution of prestress and dynamic and static stresses. The prestress is estimated from the stress drop (fig. S25) on Seg A, P, and E and is denoted as black lines for each segment (marked on top). The peak dynamic and static Coulomb stresses due to the initial branch rupture are plotted as colored curves. The purple and red dashed lines mark point I and point J, and blue and orange patches denote the subshear and supershear portions, respectively. (Inset) A graph illustrating the definition of stress parameters. (**B**) Spatial-temporal variation of dynamic Coulomb stress distribution due to initial branch rupture. The Mach wavefront is denoted as a black line. The time range used to extract triggering shear stress (8.5 to 10.5s) is marked with black dashed lines. (**C**) Map view of event 1 coseismic Coulomb stress change at 10 km depth. Other markers are fault traces of event 1 ("Evt 1," black) and event 2 ("Evt 2," green) and dislocation mechanism on receiver fault used to calculate the coseismic Coulomb stress change (top left).

the peculiar triggering sequence (Fig. 4 and figs. S34 and S35). Second, the rupture propagated from point I bilaterally at a subshear V_r (between 2.0 and 2.5 km/s). Its eastward rupture reached the junction point (point J) at ~15 s and then triggered rupture (or rerupture) of the eastern portion of Seg P at a supershear velocity (4.0 km/s). The optimized initial times and V_r values are determined from the waveforms of near-field stations (stations 05, 06, and 01; figs. S26 and S27) as well as a grid search [section S3.3 in (*18*)] to determine the optimal parameters of the FFM. The supershear rupture of Seg P continues to Seg E with a velocity of 4.0 to 4.5 km/s, as determined from FFM inversion [section S2.4 in (*18*)].

The V_r of Seg A is well constrained by the SM stations distributed along the fault, which can be used directly to measure the rupture front (Fig. 3, A and C). By making a correction of the travel times from the fault plane to the stations, we mapped the waveforms to the projection point on the fault and measured the V_r by linearly fitting the times of *S*-wave peak velocities. Waveforms in the distance-time domain indicate that rupture on Seg A initiated at about 27 s after the start of event 1 and propagated southwestward with two-stage velocities: 2.4 km/s for the initial 40 km and 3.2 km/s for the remaining 80 km (Fig. 3A and fig. S28). The averaged V_r of Seg A (3 km/s) is in the subshear regime, which is lower than the shear velocity (~3.6 km/s) during the stable second stage. We classify Seg A as a subshear rupture, although supershear may occur locally (Fig. 3A).

The bilateral V_r of event 2 was determined from the FFM inversion [section S2.4 in (*18*)], which is supershear (4.0 to 4.5 km/s) to the west direction; while its eastward V_r is 3.0 to 3.5 km/s (fig. S11F), close to the shear wave velocity. Kinematic rupture models were also obtained by several studies with various reports of rupture behaviors (*29*–*31*). We believe that our kinematic model makes considerable improvements over the previous ones by aligning the results of joint inversion of multiple datasets with direct waveform analyses [section S2.6 in (*18*)].

Triggering mechanisms and fault interactions

Our analysis shows that the kinematic rupture process varied substantially on the initial branch and the three major segments of event 1, being subshear for Seg A and supershear for the initial branch, Seg P, and Seg E. A theoretical rupture phase diagram (*32*) indicates that higher prestress on a fault tends to host supershear ruptures. We inferred that for event 1, the prestress level might have been the major factor controlling the variation in V_r, as different

Corrected 2 February 2024. See full text.

elapsed times since the last major events should have introduced various prestress levels at different segments.

We assumed a complete stress drop for all fault segments after the event and set the stress drop as prestress (τ_0) (Fig. 4). We estimated the averaged stress drop of each segment that is weighted by the mean coseismic slip [section S4.2 in (*18*)] and obtained a prestress level of 25.9, 23.9, and 14.6 MPa for Seg P, E, and A, respectively (fig. S31). By comparing the stress drop and stress loading rate [(*14*), section S4.4 in (*18*)], we also found that the ruptured portion of Seg E might not have been ruptured during the 1893 *M* 7.1 event, otherwise the elapsed time would have yielded insufficient prestress to be released by the 2023 event (fig. S36). To simulate and analyze the dynamic triggering process, we adopted elastic wave propagation and slip-weakening friction law and computed the dynamic stress field through a finite difference simulation (*27*, *28*) with the interpolated kinematic slip model [section S4.1 in (*18*)]. The stress excess ($c_0 - \tau_0$), which is defined by the difference between failing criterion (c_0) and prestress (τ_0), is regarded as the minimum stress increase required to initiate a rupture. Thus, it can be estimated from dynamic stresses for Seg P using the following derivation. Considering that the Seg P rupture was initiated at point I at about 10.5 s and that a nucleation time may be required for the rupture to grow from initial triggering to a detectable amplitude (*33*, *34*), the associated peak dynamic stress (1.4 MPa) preceding the initial rupture (8.5 to 10.5 s) is responsible for the triggering, thus it should serve as an upper bound for the local stress excess (Fig. 4A). *S* waves from the initial branch arrived at the southwest portion of Seg P at earlier times, between 8.5 and 9.5 s, yet did not trigger its rupture (Fig. 4A). Thus, peak dynamic stress between 6.5 and 8.5 s on Seg P (0.8 MPa) serves as the lower bound of the stress excess. Adding the Seg P prestress, we determine its c_0 to be between 26.7 and 27.3 MPa (Fig. 4A). Such dynamic triggering analysis is not available for the other fault segments, yet we consider the EAFZ to be a well-developed plate boundary with similar tectonic environments among segments, thus we made a first-order approximation by assuming a uniform c_0 for all segments and determined the stress excess of other segments (Fig. 4A). The associated *S* ratio (*35*), which equals $(c_0 - \tau_0)/\tau_0$, can be computed and mapped for all segments of event 1 (fig. S36). Theoretically, the dynamic V_r is related to the *S* ratio, and it is clear that the supershear segments have a substantially lower *S* ratio relative to the subshear segments, which is strong evidence that the V_r of event 1 was controlled by the prestress level—in other words, high prestress level tends to produce supershear rupture. For event 2, its stress excess is not as well constrained as in event 1, and the estimated *S* ratio also implies a prestress control of V_r during event 2 because its western-part *S* ratio is smaller than that of the eastern part (fig. S37).

We also infer that the initial-branch supershear rupture may have facilitated the supershear rupture excitation on Seg P. Numerical experiments show that the development of supershear generally needs rupture to propagate over some distance, reach the surface, or meet some stress heterogeneities to realize a transition from subshear to supershear (*32*, *36*). In our rupture kinematics, the branch Mach waves arrived at points I and J within a rather short time window (~1 s; Fig. 4), and point J was loaded with concentrated stress near the tip of the initial branch (Fig. 4A), the nucleation or initial rupture of point J might have started around 11 s. Then point J was further loaded by the point I rupture at ~15 s, which might have boosted point J rupture to a supershear velocity [section S3.3 in (*18*)]. Thus, the point I rupture might have facilitated the nucleation or rerupture of point J with extra stress loading [section S4.3 in (*18*)]. Numerical tests suggest that such a rerupturing is capable of initiating a supershear rupture (*32*). The dynamic Coulomb stress change along Seg P increased at point I between 8.8 and 10 s and decreased after the Mach wave arrival (Fig. 4B). Note that the Coulomb stress change before and after the Mach wave arrival was controlled by bulk (*P* wave) and shear (*S* wave) stress changes, respectively, thus, when considering the "direct" effect of the Mach wave (*S* wave), its shear stress inhibited ruptures on Seg P, while the dilatational stress (*37*) preceding the Mach wave was more related to the point I triggering (*33*).

We also performed a scenario earthquake simulation by assuming a subshear V_r rupture of the initial branch, leading to a much-delayed causal triggering (after 12 s; figs. S34 and S35), thus the numerical simulation performed for the kinematic process serves as a cross-validation of the point I initiation on Seg P. The numerical analysis performed in this study is based on kinematic rupture analysis adopting stress failing laws, while our conclusion of low *S* ratio and triggering sequences is also supported by a full-dynamic simulation validation (*33*, *38*). The triggering between events 1 and 2 appears to be associated with static stress instead of dynamic stress, because the events were temporally separated by 9 hours. The coseismic Coulomb stress increase produced by event 1 is about 0.1 MPa near the event 2 hypocenter, which is close to the threshold of coseismic stress triggering (Fig. 4C).

In this study, we resolved rupture behaviors of different fault segments during the 2023 Kahramanmaraş earthquake doublet. We find that initial branch triggering, multisegment rupture, and supershear rupture are three important factors related to the magnitude and damage of this event. The supershear rupture on the initial branch plays an important role in triggering and facilitating the supershear rupture of Seg P. A similar branch initiation occurred for several great continental strike-slip events (e.g., the 2001 Kokoxili, 2002 Denali, 2010 El Mayor-Cucapah, and 2016 Kaikoura earthquakes) (*2*, *16*, *39*, *40*). Such a branch initiation works as a "trigger" of a domino effect, in which a small energy release cascades into a big earthquake. Without the branch rupture, Seg P may have needed another ~80 years to accumulate enough stress to initiate its own rupture from its current loading rate (fig. S38), assuming a uniform and stable stress loading from the creeping faults at depth [section S4.4 in (*18*)]. Specifically, the initial rupture on the main fault developed near the junction between Seg A and Seg P, which was a geometrical barrier owing to fault bifurcation that might have accumulated high prestress to be released only during a large earthquake (*41*). The rupture on the initial branch sent out strong dynamic waves to the subparallel section of the main fault loaded with high prestress and triggered its subsequent rupture. Such splay branch faults are commonly associated with continental strike-slip faults, and because of their close proximities, monitoring and understanding the slip behaviors of these branches is crucial for assessing earthquake hazards of major faults.

The 2023 Kahramanmaraş doublet is also an extraordinary example of interactions between fault segments, in which a physical barrier may be breached during a large event. Previous studies suggest that supershear ruptures are more effective in jumping across fault stepovers and triggering nearby faults (*42*). Besides the cascade rupture sequence, the ground shaking intensity produced by sub- and supershear ruptures also varies substantially. For example, in a ground motion simulation of the 2023 Kahramanmaraş earthquake sequence we find that the supershear rupture increases strong shaking area (intensity above VI) by ~23% (~35,090 km^2) in comparison with a subshear scenario (fig. S39). Thus, the supershear rupture behavior influenced the damage caused by event 1 in terms of both the scope of rupture and the level of ground shaking intensity. The mainshock rupture behavior is influenced by the prestress level, which is worth particular investigation for a better understanding of faulting behaviors of continental fault zones. Earthquake scenarios that incorporate realistic prestress, multisegment rupture, and variation of V_r values are crucial for quantitatively assessing earthquake ground shaking hazards.

REFERENCES AND NOTES

1. C. Lasserre *et al.*, *J. Geophys. Res. Solid Earth* **110**, B12408 (2005).
2. D. Eberhart-Phillips *et al.*, *Science* **300**, 1113–1118 (2003).

Corrected 2 February 2024. See full text.

3. D. J. Wald, H. Kanamori, D. V. Helmberger, T. H. Heaton, *Bull. Seismol. Soc. Am.* **83**, 981–1019 (1993).
4. X. Jiang, X. Song, T. Li, K. Wu, *Earthq. Sci.* **36**, 169–174 (2023).
5. N. N. Ambraseys, *Geophys. J. Int.* **96**, 311–331 (1989).
6. T. Taymaz, J. Jackson, D. McKenzie, *Geophys. J. Int.* **106**, 433–490 (1991).
7. T. Taymaz, H. Eyidoğan, J. Jackson, *Geophys. J. Int.* **106**, 537–550 (1991).
8. T. Taymaz, J. Jackson, R. Westaway, *Geophys. J. Int.* **102**, 695–731 (1990).
9. N. Turkelli *et al*., *Geophys. Res. Lett.* **30**, 2003GL018023 (2003).
10. A. Hubert-Ferrari, R. Armijo, G. King, B. Meyer, A. Barka, *J. Geophys. Res.* **107**, ETG 9-1–ETG 9-33 (2002).
11. R. S. Stein, A. A. Barka, J. H. Dieterich, *Geophys. J. Int.* **128**, 594–604 (1997).
12. Z. Peng, Y. Ben-Zion, *Geophys. J. Int.* **160**, 1027–1043 (2005).
13. T. Y. Duman, Ö. Emre, *Spec. Publ. Geol. Soc. Lond.* **372**, 495–529 (2013).
14. L. Pousse-Beltran *et al*., *Geophys. Res. Lett.* **47**, e2020GL088136 (2020).
15. C. Zabci *et al*., *Turk. J. Earth Sci.* **20**, 411–427 (2011).
16. T. Wang *et al*., *Earth Planet. Sci. Lett.* **482**, 44–51 (2018).
17. H. Bao *et al*., *Nat. Geosci.* **15**, 942–949 (2022).
18. See supplementary materials.
19. H. Yue, T. Lay, *J. Geophys. Res. Solid Earth* **125**, e2019JB018601 (2020).
20. S. E. Güvercin, H. Karabulut, A. Ö. Konca, U. Doğan, S. Ergintav, *Geophys. J. Int.* **230**, 50–69 (2022).
21. H. Yue, Y. Zhang, Z. Ge, T. Wang, L. Zhao, *Sci. China Earth Sci.* **63**, 492–511 (2019).
22. H. Yue *et al*., *Earth Planet. Sci. Lett.* **570**, 117066 (2021).
23. H. Yue *et al*., *J. Geophys. Res. Solid Earth* **122**, 9166–9183 (2017).
24. H. Ding *et al*., *Earthq. Sci.* **36**, 417–432 (2023).
25. T. Taymaz *et al*., *Tectonophysics* **804**, 228745 (2021).
26. L. B. Freund, *Dynamic Fracture Mechanics* (Cambridge Univ. Press, 1990).
27. W. Zhang, Z. Zhang, X. Chen, *Geophys. J. Int.* **190**, 358–378 (2012).
28. W. Zhang, X. Chen, *Geophys. J. Int.* **167**, 337–353 (2006).
29. Z. Jia *et al*., *Science* **381**, 985–990 (2023).
30. C. Liu *et al*., *Nat. Commun.* **14**, 5564 (2023).
31. L. Xu *et al*., *Commun. Earth Environ.* **4**, 379 (2023).
32. J. Xu, H. Zhang, X. Chen, *Geophys. J. Int.* **202**, 2194–2206 (2015).
33. X. Ding *et al*., *Seismica* **2**, 10.26443/seismica.v2i3.1083 (2023).
34. P. Dong *et al*., *Seismol. Res. Lett.* **94**, 913–924 (2023).
35. S. Xu *et al*., *Nat. Geosci.* **16**, 94–100 (2023).
36. E. M. Dunham, P. Favreau, J. M. Carlson, *Science* **299**, 1557–1559 (2003).
37. M. Mello, H. S. Bhat, A. J. Rosakis, *J. Mech. Phys. Solids* **93**, 153–181 (2016).
38. Z. Wang *et al*., *Geophys. Res. Lett.* **50**, e2023GL104787 (2023).
39. Y. Klinger *et al*., *Bull. Seismol. Soc. Am.* **95**, 1970–1987 (2005).
40. M. Wei, D. Sandwell, Y. Fialko, R. Bilham, *Geophys. Res. Lett.* **38**, L01308 (2011).
41. Z. K. Shen *et al*., *Nat. Geosci.* **2**, 718–724 (2009).
42. R. A. Harris, S. M. Day, *J. Geophys. Res.* **98**, 4461–4472 (1993).

ACKNOWLEDGMENTS

We thank three anonymous reviewers for their constructive comments, which helped improve the article. **Funding:** This project was supported by the National Key R&D Program of China (grant 2022YFF0800602) and the National Science Foundation of China (grants 42025401, U1901602, and 42174059). T.T. acknowledges the Istanbul Technical University-Research Fund (ITU-BAP) and the Alexander von Humboldt Foundation Research Fellowship Award for providing computing facilities and other relevant resources through Humboldt-Stiftung Follow-Up Program. The Peking University research group acknowledges the China National Petroleum Corporation–Peking University Strategic Cooperation Project of Fundamental Research. **Author contributions:** C.R. constructed the fault model and performed MPS and FFM inversion. Z.W. conducted waveform-based analysis of the kinematics. N.H. and W.Z. performed wavefield simulation. Z.Z. conducted the stress analysis. All authors contributed to the initial draft of the manuscript. H.Y. and X.S. conceived of and administrated the project, guided the scientific discussion, wrote most of the manuscript, and acquired the funding. Z.S. contributed to the scientific discussion and manuscript editing. H.L., T.W., Z.L., and Hang Xu processed the SAR and optical images and contributed to manuscript writing on SAR data processing. T.T., T.S.I., and C.E. collected continuous local and regional broadband seismograms, strong ground motion waveforms, and GPS and high-rate GPS data and contributed to manuscript editing and interpretation of the active tectonics of Eastern Anatolia, Türkiye. J.G. processed the original GPS data. Haoyu Xu, Z.G., Y.Z., H.D., and B.C. contributed to the hypocenter relocation of the mainshocks and the aftershock catalog. **Competing interests:** The authors declare that they have no competing interests. **Data and materials availability:** The teleseismic data were download from IRIS (https://www.iris.edu/hq/). The strong motion waveforms were retrieved from AFAD (https://tdvms.afad.gov.tr/event_spec_data). The GPS data were provided by the CORS-TR (TUSAGA-Aktif: https://www.tusaga-aktif.gov.tr) GNSS network administrated by the General Directorate of Land Registry and Cadastre (TKGM) and General Directorate of Mapping (HGM-Ankara, Türkiye). The Sentinel-1 SAR data and Sentinel-2 optical data were provided by the European Space Agency (https://scihub.copernicus.eu), and the Sentinel-1 data were distributed by the Alaska Satellite Facility (https://asf.alaska.edu/how-to/data-tools). The Advanced Land Observation Satellite-2 (ALOS-2) SAR data used in this work are under the copyright of the Japan Aerospace Exploration Agency (JAXA) and were openly accessed at https://www.eorc.jaxa.jp/ALOS/en/dataset/alos_open_and_free_e.htm.

SUPPLEMENTARY MATERIALS

science.org/doi/10.1126/science.adi1519
Supplementary Text
Figs. S1 to S39
Tables S1 to S13
References (*43*–*73*)
Slip Models of Events 1 and 2

Submitted 15 April 2023; accepted 5 December 2023
10.1126/science.adi1519